Tackling the Activity and Selectivity Challenges of Electrocatalysts towards Nitrogen Reduction Reaction via Atomically Dispersed Bi-Atom Catalysts

Xiangyu Guo[†], Jinxing Gu[§], Shiru Lin[§], Shengli Zhang[‡,*], Zhongfang Chen[§,*], Shiping Huang[†,*]

[†] State Key Laboratory of Organic-Inorganic Composites, Beijing University of Chemical Technology, Beijing 100029, China

[§] Department of Chemistry, University of Puerto Rico, Rio Piedras, San Juan, PR 00931, USA

[‡] MIIT Key Laboratory of Advanced Display Materials and Devices, Ministry of Industry and Information Technology, Institute of Optoelectronics & Nanomaterials, Nanjing University of Science and Technology, Nanjing 210094, China

ABSTRACT

Developing efficient catalysts for nitrogen fixation is becoming increasingly important, but is still challenging due to the lack of robust design criteria to tackling the activity and selectivity problems, especially for electrochemical nitrogen reduction reactions (NRR). Herein, by means of large-scale density functional theory (DFT) computations, we reported a descriptor-based design principle to explore the large composition space of two-dimensional (2D) bi-atom catalysts (BACs), namely metal dimers supported on 2D expanded phthalocyanine (M_2-Pc or MM'-Pc), towards NRR at the acid conditions. We sampled both homonuclear (M_2-Pc) and heteronuclear (MM'-Pc) BACs, and constructed the activity map of BACs by using N_2H^* adsorption energy as the activity descriptor, which reduces the number of promising catalyst candidates from over 900 to less than 100. This strategy allowed us to readily identify three homonuclear and 28 heteronuclear BACs, which could break the metal-based activity benchmark towards efficient NRR. Particularly, using the free energy difference of H* and N_2H^* as selectivity descriptor, we screened out five systems, including Ti_2-Pc, V_2-Pc, TiV-Pc, VCr-Pc, and VTa-Pc, which exhibit a strong capability of suppressing the competitive hydrogen evolution reaction (HER) with favorable limiting potential of −0.75, −0.39, −0.74, −0.85 and −0.47 V, respectively. This work not only broadens the possibility of discovering more efficient BACs towards N_2 fixation, but also provides a feasible strategy for rational design of NRR electrocatalysts, and help pave the way to fast screening and design of efficient BACs for NRR and other electrochemical reactions.

1. INTRODUCTION

Direct reduction of nitrogen (N_2) into ammonia (NH_3) represents one of the most important, yet challenging, chemical transformations. Currently, most ammonia is synthesized by the preeminent Haber-Bosch process, which uses around 1-2% of man-made energy supply, and releases about 1.44 % of global CO_2 emissions.[1] Thus, it is of paramount importance to find economical and environmentally friendly routes for nitrogen fixation.

As the alternative of Haber-Bosch process, electrochemical N_2 fixation holds the great promise of directly converting abundant N_2 and renewable electricity into NH_3 in aqueous solutions at ambient conditions of temperature and pressure.[2-8] Unfortunately, the corresponding N_2 reduction reaction of this electrochemical process (NRR: $N_2 + 6H^+/e^- = 2NH_3$) suffers from activity and selectivity problems, due to the sluggish kinetics and the competing hydrogen evolution reaction (HER) in the aqueous solutions.[9-15] Specifically, the Faradaic efficiency (FE) values, which describe the percentage of charges transferred in a system facilitating the target reaction, are very small (typically ranging from less than one to several tens of percent) when NRR is catalyzed by metals,[16-22] metal oxides,[23-25] transition metal chalcogenides,[26-27] and other metal-free materials.[28-34] Therefore, it is highly desirable to develop stable, active, and low-cost electrocatalysts with high FE values for further advancing the electrochemical NRR technology.

The newly emerging atomically dispersed catalysts, e.g., single-atom catalysts (SACs), are of particular interest due to their high atom utilization and exceptional

catalytic performances.[35-39] Theoretically, many SACs, such as Mo-BN,[40] Fe-graphene,[41] Ru-g-C_3N_4,[42] and single-boron catalysts,[43-45] were predicted as high-performance NRR catalysts. Experimental studies revealed that some SACs can suppress HER to some extent, and thus are capable of improving FE.[46-49] For example, anchoring the single Ru atom onto the nitrogen-doped carbons can achieve high FE of 29.6% at −0.2 V vs. reversible hydrogen electrode.[50] However, since NRR involves multiple reaction intermediates, it is rather challenging for the single-atom center to simultaneously improve the yield rate and FE. To address this issue, a promising strategy is to introduce dimer sites to tune the adsorption of intermediates. Such bi-atom catalysts (BACs), with more flexible active sites and synergetic interatomic interactions, can maximize the potentials of the SACs for multistep reactions, which provides a feasibility to optimize activity and selectivity.[51-56] For example, the Pt_2 dimers well dispersed on graphene catalyzed the hydrolytic dehydrogenation of ammonia borane at a specific rate nearly 17-fold higher than the isolated single Pt atoms.[57] Theoretically, Co, Ni, and Cu-based BACs have been predicted to have much higher activity towards O_2 reduction, as compared with their single-atom counterparts.[58-59] For NRR, several metal dimers, including Mo_2 and Mn_2, supported by 2D C_2N monolayer, were predicted to have better catalytic activity than that of the corresponding SACs.[60-61]

Note that so far most efforts in electrocatalyst design primarily focus on the homonuclear BACs. However, in principle, there exist myriad of possible combinations for heteronuclear dimers, since mixing the 3d, 4d, and 5d and main group metals together could produce more than 900 candidates at one specific support with

asymmetric adsorption sites.[62-70] Therefore, it is imperative to establish a feasible strategy, which can enable the rational design of stable, active, and in particular highly selective electrocatalysts towards NRR, and better bridge the gap between theory and experiments.

To conquer this challenge, especially to simultaneously achieve high activity and high selectivity for NRR, in this work, we adopted a descriptor-based design principle and demonstrated its validity in screening and designing two-dimensional (2D) electrocatalysts for NRR. By means of large-scale systematic density functional theory (DFT) computations and taking the 2D expanded phthalocyanine (Pc) substrate as an example, we built up the full profile of the stability, activity, and selectivity of metal dimers anchored on 2D Pc towards NRR at the acid conditions, and sampled the large composition space of both homonuclear (M_2-Pc) and heteronuclear (MM'-Pc) BACs. We demonstrated that three homonuclear BACs and 28 heteronuclear BACs could break the metal-based activity benchmark and achieve the efficient N_2 electroreduction. Specifically, the HER, which is the most problematic yet dominate side reaction in NRR, can be dramatically suppressed on the Ti_2-, V_2-, TiV-, VCr-, and VTa-Pc BACs with the less negative limiting potential of −0.75, −0.39, −0.74, −0.85 and −0.47 V, which are more favorable than most reported electrocatalysts for NRR. This work provides a comprehensive understanding of stability, activity and selectivity of BACs, which could guide further exploration of an even broader composition space of BACs for NRR or other related reactions.

2. COMPUTATIONAL METHODS

All the computations were carried out by spin-polarized DFT method including van der Waals (vdW) corrections, as implemented in Vienna ab initio Simulation Package (VASP).[71-72] The exchange correlation energy was modelled by Perdew-Burke-Ernzerhof (PBE) functional within the generalized gradient approximation (GGA).[73] An energy cutoff of 400 eV was adopted for the plane-wave basis. In structural optimizations, the Brillouin zone was sampled by 3×3×1 *k*-points using Monkhorst-Pack scheme, while a denser *k*-points of 9×9×1 was employed for electronic property computations. To avoid interactions between periodic images, a vacuum space of 15 Å was used in the perpendicular direction of the 2D layer. The energy and force convergence thresholds for the iteration in self-consistent filed (SCF) were set to 10^{-5} eV and 0.02 eV/Å, respectively. Since the solvation-induced stabilization of reaction intermediates in NRR is within 0.2 eV (affecting the limiting potential for NRR by ~0.1 eV),[74] the effects of solvation were not taken into account. The free energy diagram of NRR was obtained by referring to the computational hydrogen electrode (CHE) model proposed by Nørskov *et al.*.[75] More computational details regarding electrochemical reactions and surface models are given in the Supporting information.

3. RESULTS AND DISCUSSION

3.1. Structural Models of BACs

Experimentally, metal dimers have been successfully anchored on various 2D materials, such as graphene,[76] graphitic carbon nitride (g-C_3N_4),[77-78] nitrogen-doped carbons,[79-80] and rectangular-shaped expanded phthalocyanine,[81] to form the BACs. In these cases, the metal atoms can either be trapped at the graphene trivacancy,

quadrovacancy, and two adjacent single vacancies, or coordinate with nitrogen/carbon atoms to form metal-carbon/nitrogen moieties (**Figure S1)**. Using one of the experimentally available Fe dimers as the prototype,[55] we found that the binding strength between the metal dimers and substrates can be significantly affected by the coordination environment of metals. Especially, the phthalocyanine (Pc) family serves as probably the best substrate for us to investigate BACs due to the flexibility of the physical-chemical and catalytic properties, as well as the strong binding for the metal atoms. Thus, in this study, we built up the repository of Pc-based BACs, namely M_2-Pc and MM'-Pc.

In M_2-Pc (or MM'-Pc), four isoindole rings are connected by two methanetriamine moieties, which accommodate two metal atoms in the central cavity (**Figure 1a**); each metal atom combines with two pyrrole nitrogen atoms and two amino nitrogen atoms of the macrocycle to form the M_2N_6 moiety. In principle, all the 3d, 4d, 5d, and main group metal atoms can serve as the metal centers of M_2-Pc (or MM'-Pc). However, due to the toxic/radioactive nature, Tc, Cd, Hg, In, Tl and Pb were excluded in this study. We only considered 30 metal atoms, including 27 transition metal atoms (except for lanthanides, Tc, Cd, and Hg) and three main group metal atoms (Al, Ga, Bi) as the central atoms in the 2D phthalocyanine networks. We will first focus on understanding the stability and activity of homonuclear BACs, then extend the modeling capabilities to capture greater complexities of heteronuclear BACs.

3.2. Homonuclear BACs

3.2.1 Structure and Stability

First, we theoretically investigated the geometric structures of the above mentioned 30 homonuclear M_2-Pc monolayers (**Figure 1a**, the details of the optimized structures and the corresponding structural parameters are given in **Figure S2** and **Table S1** of Supporting Information). In the optimized structures, the central atoms are in or out of the Pc plane, mostly depending on the radii of the metal atoms. Ten metal atoms, namely Al, Cr, Mn, Fe, Co, Ni, Ru, Rh, Os, and Ir, can incorporate into the central cavity of Pc and form the almost in-plane configurations, whereas the remaining 20 dimers slightly protrude out of the Pc plane, leading to the buckled structures. The distances between two metal atoms are in the range of 2.30 (for Fe_2-Pc) and 3.41 Å (for Bi_2-Pc). Compared with the interatomic distances in the bulk, Cr_2, Ni_2, Cu_2, Pd_2, Pt_2. Sn_2, and Bi_2 display longer bond length, while the other metal dimers have shorter distances (**Table S1**, **Figure S3**). Such interconnection enables the metal dimers to respond cooperatively to adsorbate with communicative structural self-adaption and electronic transformation,[82] which induces different catalytic performance from that of single-atom counterparts.

Then, we evaluated the thermodynamic and electrochemical stabilities of these 30 M_2-Pc monolayers by the formation energy E_f and dissolution potential U_{diss} (**Figure 1b**),[83] which are defined as

$$E_f = (E_{M_2-Pc} - E_{Pc} - 2E_M)/2 \qquad (1)$$

$$U_{diss} = U^{\circ}_{diss}(metal, bulk) - {}^{E_f}/_{ne} \qquad (2)$$

where E_M is the total energy of metal atom in its most stable bulk structure, E_{M_2-Pc} and E_{Pc} are the total energies of M_2-Pc and substrate, $U_{diss}^{\circ}(metal, bulk)$ and n are the standard dissolution potential of bulk metal and the number of electrons involved in the dissolution, respectively. According to our definition, systems with $E_f < 0\ eV$ are considered to be thermodynamically stable, while materials with $U_{diss} >$ 0 V vs. SHE. are regarded as electrochemically stable. The exact values of E_f and U_{diss} are listed in **Table S2**. Note that most of the experimentally synthesized SACs are thermodynamically and electrochemically stable according to our above evaluation criteria (**Figure S4)**,[84] which suggests the reliability and feasibility of our approach.

Promisingly, the computed E_f of all the considered M_2-Pc systems are well below zero, suggesting high thermodynamic stabilities of these metal dimers on the Pc substrate. As far as the U_{diss} is concerned, five systems, namely Sc_2-Pc, Y_2-Pc, Zr_2-Pc, Nb_2-Pc, and Hf_2-Pc, are ruled out due to the electrochemical instability at the acid conditions, as indicated by their negative U_{diss} values. Thus, we finally screened out 25 homonuclear M_2-Pc that meet the stability criteria for further investigations.

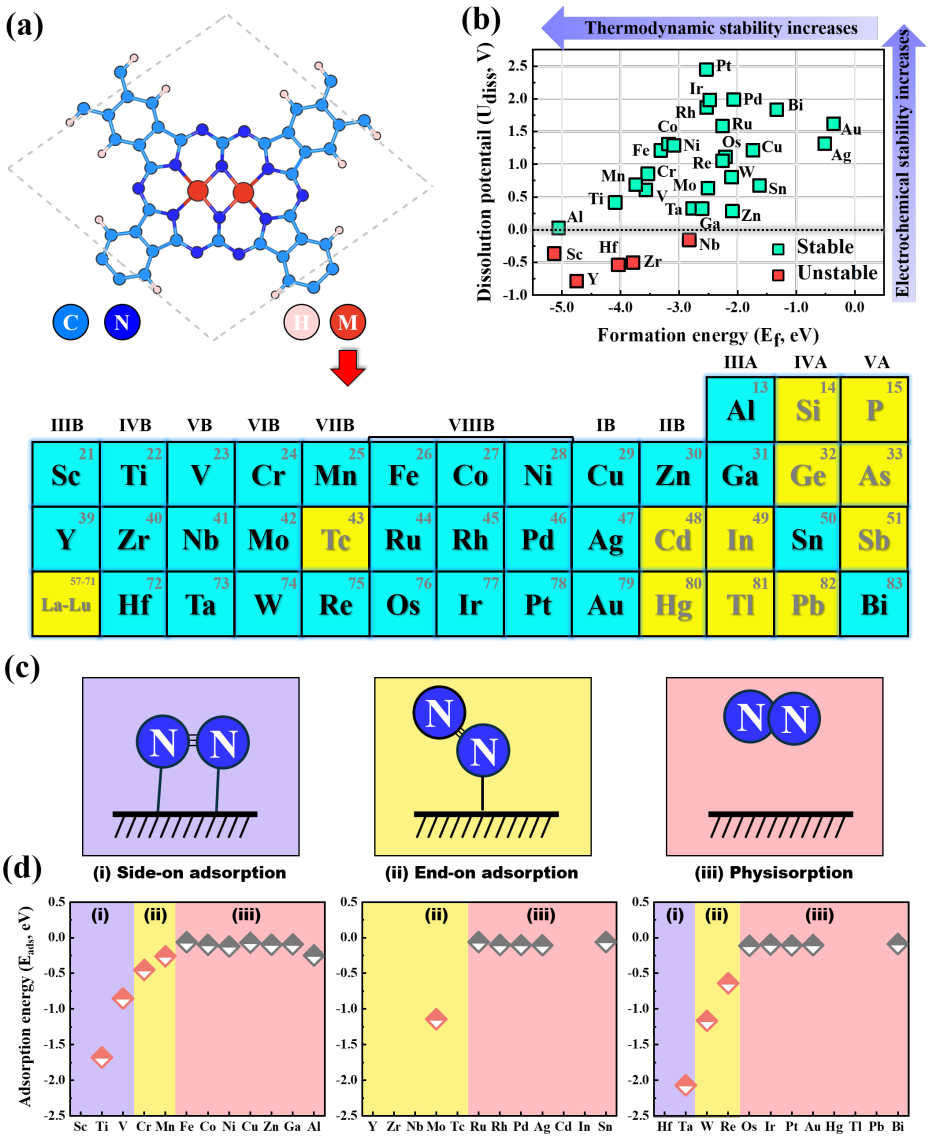

Figure 1. (a) Structural prototype of 2D M_2-Pc nanosheet. (b) Computed formation energy and dissolution potential of metal atoms in M_2-Pc. (c) Three possible configurations of N_2 on M_2-Pc surfaces. (d) Computed adsorption energies of N_2 on M_2-Pc surfaces and the N_2 adsorption configurations.

3.2.2 N_2 Adsorption

Under ambient conditions, N_2 can be electrochemically reduced to NH_3/NH_4^+ following distal,[85] alternative,[86] enzymatic,[87] and mixed pathways[88] on a catalyst surface. A key step in the proposed mechanisms is the adsorption and activation of the classically inert N_2. Thus, we investigated the N_2 adsorption on the 25 homonuclear M_2-Pc.

These 25 M_2-Pc can be divided into three categories depending on the adsorption configuration of N_2 (**Figure 1c**): the N_2 may interact with the M_2-Pc either through physisorption, or through chemisorption via side-on/end-on configurations.

Our computations demonstrated that 17 M_2-Pc (M = Al, Fe, Co, Ni, Cu, Zn, Ga, Ru, Rh, Pd, Ag, Sn, Os, Ir, Pt, Au, and Bi) interact with M_2-Pc only by physisorption. The computed adsorption energy (E_{ads}) on these catalysts are close to 0 eV, indicating that the adsorption and activation of N_2 on these M_2-Pc hardly take place at room temperature (**Figure 1d**).

In contrast, N_2 chemisorption occurs on eight M_2-Pc (M= Cr, Mn, Mo, W, Re, Ti, V, and Ta) with E_{ads} values between −0.26 and −2.07 eV. N_2 can be readily adsorbed on Cr_2-Pc, Mn_2-Pc, Mo_2-Pc, W_2-Pc, and Re_2-Pc via end-on configuration, whereas side-on adsorption is preferred on Ti_2-Pc, V_2-Pc, and Ta_2-Pc surfaces. Charge density difference plots indicate that upon adsorption, the adsorbed N_2 can interact with these eight M_2-Pc by the so-called "push-pull" hypothesis, in which M_2-Pc can "push" electrons into the antibonding orbitals of N_2 and simultaneously "pull" the lone-pair electrons from the N_2 (**Figure 2**). Especially, since the occupied orbitals of metal atoms

can "push" electrons into antibonding orbitals of N_2 via both two N atoms, Ti_2-Pc, V_2-Pc, and Ta_2-Pc, which possess the side-on configuration, can remarkably activate the N≡N bond, leading to the significant N_2 bond elongation (1.19~1.22 Å, vs. 1.12 Å in free gas phase).

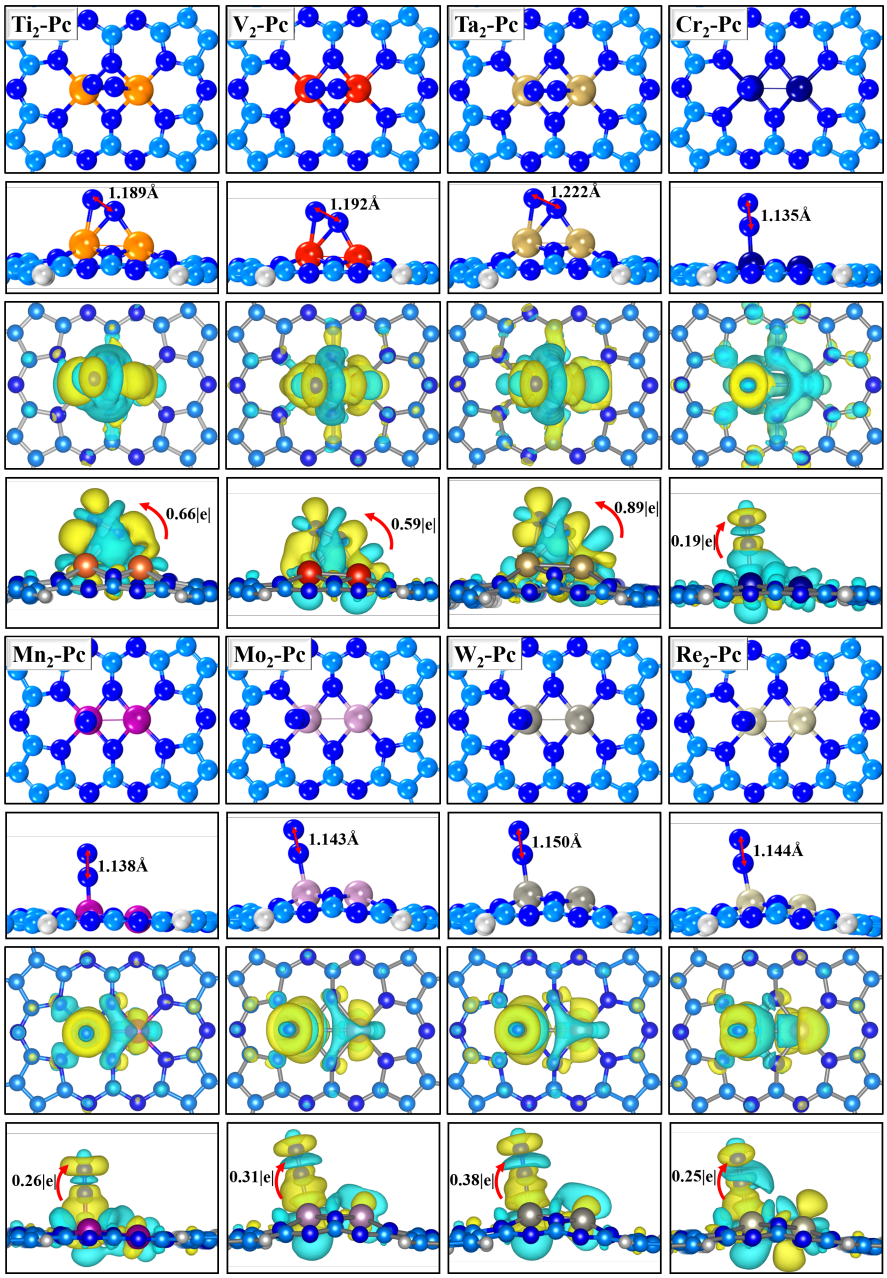

Figure 2. Optimized adsorption configurations and charge density differences of N_2 chemisorbed on eight M_2-Pc surfaces. The charge depletion and accumulation were depicted by cyan and yellow, respectively. The isosurface value is 0.003 e/Å^3.

To understand the underlying mechanism of the N_2 activation, we analyzed the interactions between the metal dimers and N_2 by plotting the partial density of states (PDOS) (**Figure 3**) of their energetically most favorable configurations. Compared with the molecular orbitals of free N_2, the strong ability for M_2-Pc to adsorb/activate N_2 is primarily associated with their availability of unoccupied and occupied *d* orbitals. On one hand, the unoccupied *d* orbitals of M_2-Pc accept electrons from the 2π and 3σ molecular orbitals of N_2, forming the bonding states to strengthen the N_2 adsorption. On the other hand, the occupied *d*-orbitals of metal dimers back-donate electrons to the $2\pi^*$ orbital of N_2, leading to the partially occupied $2\pi^*$ orbital near the Fermi level. The strong d-$2\pi^*$ coupling can activate the adsorbed N_2 to be radical-like, which is ready for hydrogenation.

To gain deep insights into the d-$2\pi^*$ interaction quantitatively, we performed the integrated-crystal orbital Hamilton population (ICOHP) analysis by integrating the band states up to the highest occupied energy level (**Figure 3**).[89] Note that a more negative value of ICOHP implies a stronger d-$2\pi^*$ coupling. The computed ICOHPs for those with side-on N_2 adsorption configurations (−0.92, −0.95, and −1.33 for Ti_2-Pc, V_2-Pc, and Ta_2-Pc, respectively) are more negative than those with end-on N_2 adsorptions (−0.55, −0.57, −0.73, −0.73, and −0.74 for Cr_2-Pc, Mn_2-Pc, Mo_2-Pc, W_2-Pc, and Re_2-Pc, respectively). More interestingly, we plotted the ICOHP versus the Gibbs free energy change of the first hydrogenation step ($N_2^* \rightarrow NNH^*$), and found an approximately linear correlation with R^2 of 0.78 (**Figure S5**), suggesting the important role of adsorption configurations for N_2 activation. This characteristic could also well

explain why 10 candidates out of 270 SACs, which were predicted with high NRR activity, prefer to adsorb N_2 through the side-on configuration.[90] However, since the catalytic activity of NRR is governed by multiple reaction intermediates, the detailed reaction pathways and activity trends will be systematically evaluated in the next section.

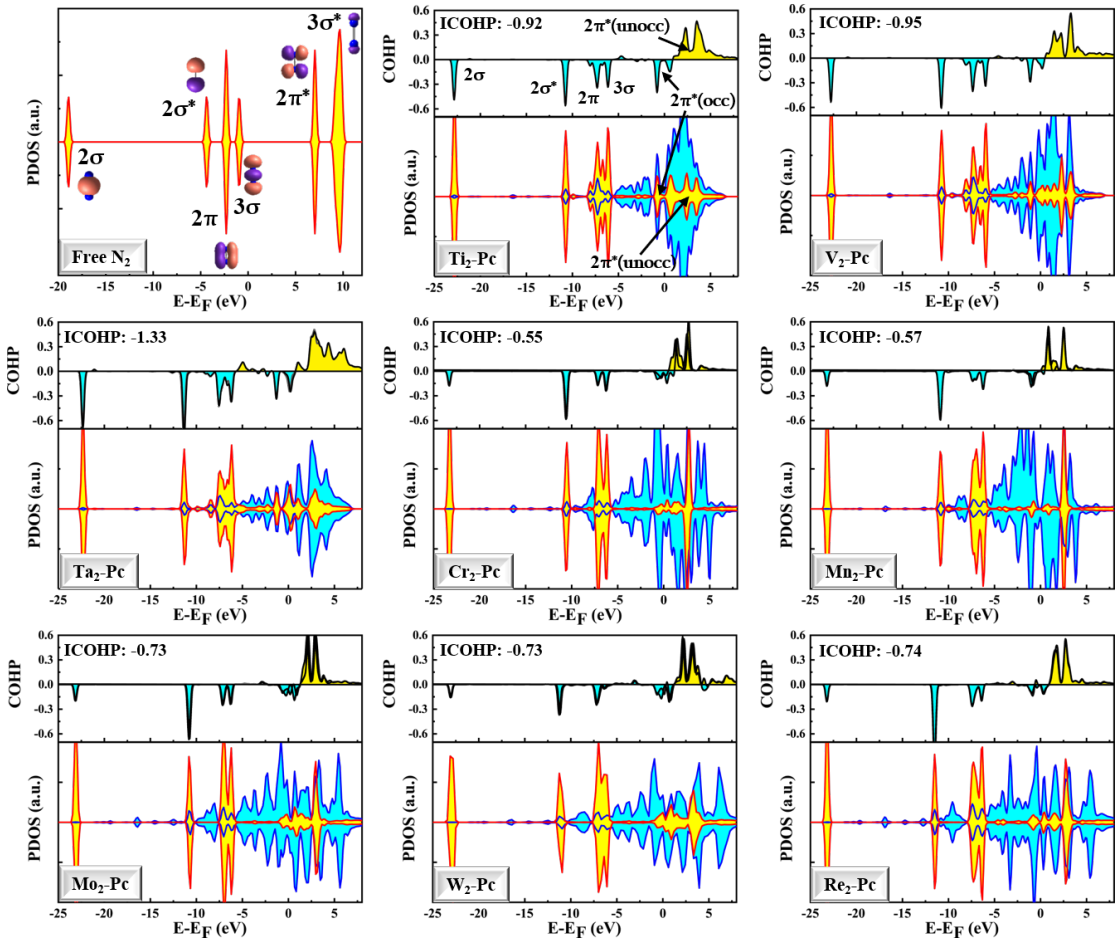

Figure 3. Molecular orbitals of free N_2, and the computed partial density of states (PDOS) and the integrated crystal orbital Hamilton populations (ICOHP) of N_2 on eight M_2-Pc (M=Ti, V, Ta, Cr, Mn, Mo, W, and Re) surfaces. The bonding and antibonding states in ICOHP are depicted by cyan and yellow, respectively.

3.2.3 Catalytic Activity of Homonuclear BACs

Theoretically, the intrinsic activity of the electrocatalysts can be estimated by the limiting potential (U_L) or overpotential. Note that the products of NRR are pH-dependent (**Figure 4a**), the overpotential can be affected by conditions of electrolyte. Thus, we used U_L to evaluate the activity trends for different materials, and the corresponding U_L on stepped Ru(0001) (cat. −0.98 V) was set as the metal-based benchmark due to the highest theoretical activity among bulk metal surfaces.[91-92] Accordingly, M_2-Pc with less negative (or more positive) U_L related to that of stepped Ru(0001) ($U_L > -0.98$ V) are considered to possess improved catalytic activity towards NRR.

Figure 4b summarizes the U_L values for 25 homonuclear M_2-Pc which meet the stability criteria. Notably, three systems, including Ti_2-Pc, V_2-Pc, and Re_2-Pc, can co-balance the adsorption for the multiple reaction intermediates, which display outstanding activity towards NRR as compared to the stepped Ru(0001) surface, with more favorable U_L values of −0.75 V, −0.39 V, and −0.82 V, respectively. Whereas for Ta_2-Pc, the intrinsic activity is limited due to its strong interaction with the adsorbates.

Four possible associative NRR catalytic mechanisms, namely distal, alternative, enzymatic, and mixed, are possible on the most promising M_2-Pc (M= Ti, V, Re) catalysts, as schematically illustrated in **Figure 4c**. Due to the high energy barrier of N_2 dissociation (e.g., 2.94 eV on Ta_2-Pc, **Figure S6**), the dissociative mechanism for N_2 fixation was not considered. The free energy diagrams of NRR on these three M_2-Pc

are presented in **Figure 4d-f**, while the computed thermodynamic properties and the optimized structures of reaction intermediates are given **Table S3-5** and **Figure S7-S9**, respectively.

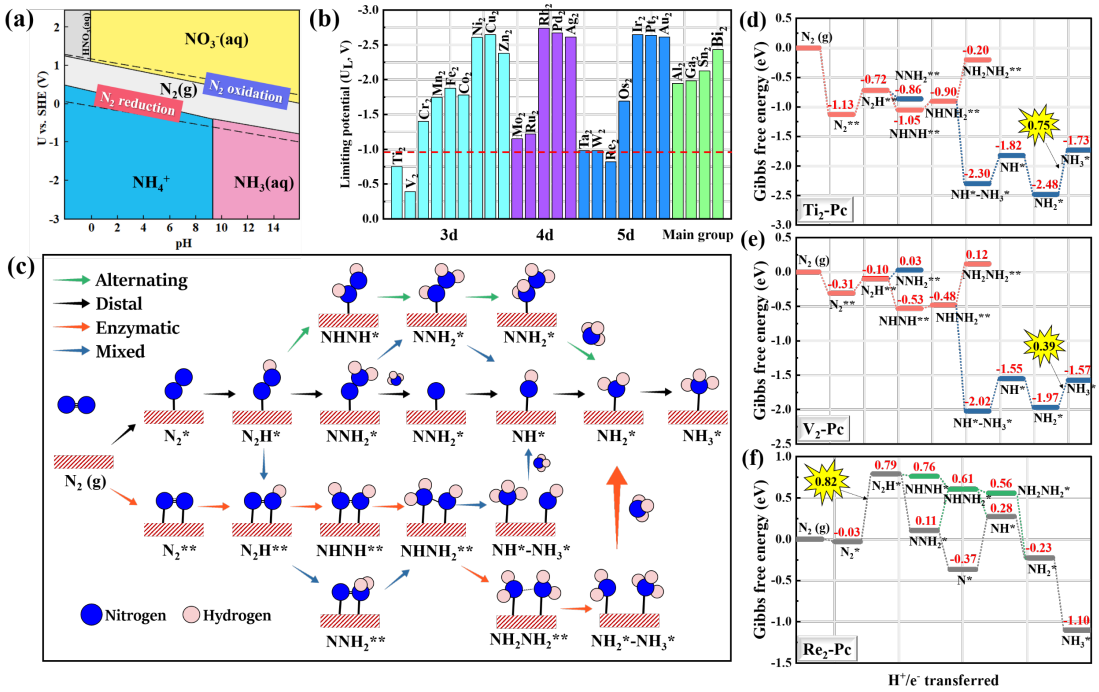

Figure 4. (a) Pourbaix diagram of the N_2-H_2O system. (b) Theoretical limiting potential U_L for 25 homonuclear M_2-Pc screened out by stability analysis. (c) Schematic illustration of the possible reaction mechanisms during the N_2 reduction. (d)-(f) Gibbs free energy diagrams for N_2 electroreduction on Ti_2-Pc, V_2-Pc and Re_2-Pc, respectively.

First, we investigated the NRR pathway on Ti_2-Pc and V_2-Pc since N_2 prefers side-on configuration on these two catalysts. In the reduction process, the adsorbed N_2 (N_2*) can interact with H^+/e^- pair to form the NNH*. The Gibbs free energy changes of the first hydrogenation step (N_2* → NNH*) on Ti_2-Pc and V_2-Pc are 0.41 and 0.21 eV, respectively. Then, the H^+/e^- pair can attack one N atom of the adsorbed N_2H species

to form the NHNH* or NNH_2* intermediate. Comparing the Gibbs free energy change in these two elementary steps, we found that Ti_2-Pc and V_2-Pc prefer to catalyze NRR through the N_2H* → NHNH*, whereas the formation of NNH_2* could be much hindered due to the more positive free energy change. Subsequently, the NHNH* can be readily hydrogenated into $NHNH_2$* after overcoming a small potential barrier (0.15, and 0.05 eV for Ti_2-Pc and V_2-Pc respectively). In the following steps, the protonation of $NHNH_2$* can proceed via $NHNH_2$* → NH*-NH_3*, and the generation of second NH_3 (NH_2* →NH_3*) was identified as the potential-limiting step (PDS) (with the maximum free energy change of 0.75 and 0.39 eV, respectively). Simply, we can compute the U_L value using the equation $U_L = -{\Delta G_{PDS}}/{e}$, and the corresponding U_L for Ti_2-Pc and V_2-Pc are −0.75 and −0.39 V, respectively. Hence, after applied a U_L on Ti_2-Pc and V_2-Pc surfaces, all the electron-transfer steps can be downhill, favoring the production of NH_3, and the reaction process follows the enzymatic and mixed mechanism. Moreover, we also examined the kinetics of the proton transfer in PDS using the Zundel $H_5O_2^+$ as the solvated proton donor (**Figure S10**). The computed activation barriers of PDS at the 0.0 V versus SHE are only 0.38 and 0.35 eV, respectively, on the Ti_2-Pc and V_2-Pc catalysts. Such small barries can be easily surmountable at room temperature or diminished with more negative applied voltages.

Then, we examined the NRR pathway on Re_2-Pc where N_2 adopts end-on configuration. Similar to the other two catalysts, NNH* is formed by the interaction between N_2* and H^+/e^- pair, and this hydrogenation step (N_2* → NNH*) is 0.82 eV uphill in the free energy profile. Afterwards, the N_2H* is easily protonated by H^+/e^- pair,

releasing energy of 0.68 eV and leading to the energetically more favorable NNH_2* (rather than NHNH*, which is 0.65 eV higher in energy). Once the NNH_2* is formed, the first NH_3 molecule can be readily desorbed on the catalyst surface, leaving a single nitrogen atom on the Re site. In the subsequent reaction steps, three H^+/e^- pair can continuously attack the remaining N*, forming the NH*, NH_2* and NH_3* with an energy demand of 0.65, −0.51 and −0.87 eV, respectively. Among all the elementary steps, the formation of N_2H* (N_2* → NNH*) is the PDS with the maximum free energy change of 0.82 eV. Thus, when the external potential increases to −0.82 V, the free energy of PDS becomes zero, and the electron-transfer steps can be proceeded by the distal mechanism.

Noteworthily, different from the NRR under strong alkaline conditions or thermal catalysis, in which the desorption of NH_3* plays an important role in the whole process, the protonation of NH_3* into NH_4^+ trends to be facile under the acid or alkalescence conditions, [93-94] and thus was not examined in detail (the computed adsorption energies of NH_3* on BACs are given in **Table S6**).

To summarize, among the 25 homonuclear M_2-Pc, we identified that Ti_2-Pc, V_2-Pc, and Re_2-Pc exhibit higher activity towards NRR than the stepped Ru(0001) surface. Particularly, V_2-Pc displays most less negative U_L value of −0.39 V, which is more favorable than that of Ti_2-Pc (−0.75), Re_2-Pc (−0.82), and reported B-C_3N_4 (−0.47 V),[43] Mo-C_2N (−0.53 V),[95] Mo-graphdiyne (Mo-GDY, −0.99 V)[49], Ru-N_3 (−1.10 V),[50] Ru-NC_2 (−0.82 V), and Ru-ZrO_2 (−1.41 V)[96] catalysts under the same theoretical level (the computed thermodynamic properties are listed in **Table S7**).

3.3. Exploration of Heteronuclear BACs for NRR

The above activity data enabled us to find descriptors to build up a full activity picture of the M_2-Pc and MM'-Pc systems. Once the activity trends are identified, it can be used to create a candidate list of all the combinatorial possibilities of heteronuclear BACs.

First, we employed two previously selected descriptors, the adsorption energy of NNH* ($\Delta E_{N_2H^*}$) and $\Delta E_{NH_2^*}$, to describe the catalytic behavior of M_2-Pc and MM'-Pc systems.[37, 74, 90, 91] Interestingly, we found the volcano-shaped relationship between the theoretical limiting potential (U_L) and $\Delta E_{N_2H^*}$ (**Figure 5a**), in which the best limiting potential occurs when $\Delta E_{N_2H^*}$ is close to −1.0 eV, whereas the correlation between the limiting potential and the NH_2* adsorption energy is less satisfactory than that between the limiting potential and the N_2H* adsorption energy, as illustrated in **Figure S11**. When $\Delta E_{N_2H^*}$ on the catalyst is stronger than ca. −1.0 eV ($\Delta E_{N_2H^*}$< ~−1.0 eV, left branch in **Figure 5a**), for example, Ti_2-Pc and Ta_2-Pc, the NNH* can be readily formed, but the interaction between NH_2* and catalyst is so strong that the formation of NH_3* is difficult to achieve. On the contrary, when the $E_{N_2H^*}$ is weaker than ca. −1.0 eV ($\Delta E_{N_2H^*}$>~ −1.0 eV), the N_2* + H^+/e^- → NNH* step is difficult to proceed. To balance these two requirements, the $\Delta E_{N_2H^*}$ for an active catalyst should be near −1.0 eV. Note that the V_2-Pc, which displays the highest activity among all the considered homonuclear M_2-Pc, is located near the peak of the volcano with $E_{N_2H^*}$ of -0.99 eV. Thus, $\Delta E_{N_2H^*}$ can be used as a good activity descriptor for us to screen efficient BACs towards NRR. More interestingly, the previously studied 2D C_2N-supported Mn_2 and

Mo_2 BACs also follow the general tendency of our volcano-shaped relation, implying that the constructed scaling relations could be used to other types of BACs.[60-61]

To better understand the possible relations between $\Delta E_{N_2H^*}$ and electronic properties of metal dimers, we also plotted the correlations between the N_2H adsorption energy ($\Delta E_{N_2H^*}$) and (*i*) the band center of adsorbed metal atoms (**Figure S12a**),[97] and (*ii*) the energy of lowest unoccupied state of 25 homonuclear bi-atom catalysts (**Figure S12b**).[98] Unfortunately, no strong correlation between $\Delta E_{N_2H^*}$ and the two other potential descriptors were found. This finding is likely due to the different band hybridization of N_2H* on different metal surfaces, which is similar to our recent study.[84] For metal atoms with strong binding for the N_2H*, the adsorption energy can be significantly affected by the band center of metal atoms because of the strong band hybridization between the metal and N_2H*. However, for the systems with weak binding with N_2H*, the adsorption is mainly associated with the charge transfer between the metal and adsorbates.

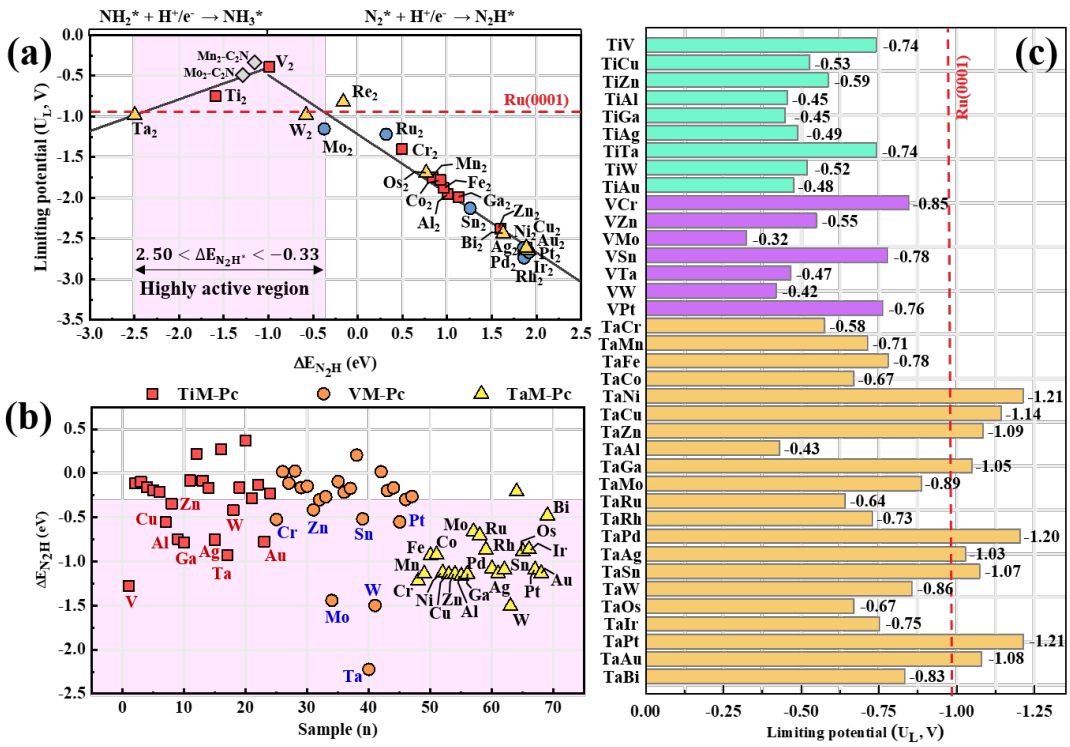

Figure 5. (a) Volcano-shaped relationship between the theoretical limiting potential (U_L) and the adsorption energy of N_2H^* intermediate ($\Delta E_{N_2H^*}$). (b) Variations of $\Delta E_{N_2H^*}$ on 69 heteronuclear M_2-Pc. (c) Summary of U_L values on 37 heteronuclear M_2-Pc catalysts which were proposed as promising catalysts by using $\Delta E_{N_2H^*}$ as the activity descriptor. The Ti-, V-, and Ta-based BACs are depicted by aqua, violet, and yellow, respectively.

Using the $\Delta E_{N_2H^*}$ as the activity descriptor, we extended our study to 69 heteronuclear MM'-Pc by mixing one of the metal atoms in the left branch of the volcano-type plot (i.e. Ta, Ti, and V with N_2H^* binding strength stronger than −1.0 eV) with the remaining 24 metal atoms (**Figure 5b**). We expect that the binding strength of multiple reaction intermediates could be tuned by doping Ta/Ti/V with another metal atom that has a weaker binding to the N_2H intermediate, consequently the activity

toward NRR could be improved. Given that the $\Delta E_{N_2H^*}$ value for an active catalyst is typically in the range of −0.33 and −2.50 eV as revealed from the scaling relations, 37 of 69 heteronuclear MM'-Pc were proposed as promising candidates, and further examined by detailed activity analyses (**Figure 5c**, the computed $\Delta E_{N_2H^*}$, U_L and corresponding PDS can be found in **Table S8**). Finally, our DFT computations identified 28 heteronuclear BACs, including nine Ti-based BACs (TiV, TiCu, TiZn, TiAl, TiGa, TiAg, TiTa, TiW, TiAu), seven V-based BACs (VCr, VZn, VMo, VSn, VTa, VW, VPt), and 12 Ta-based BACs (TaCr, TaMn, TaFe, TaCo, TaAl, TaMo, TaRu, TaRh, TaW, TaOs, TaIr, TaBi), with intrinsic activity better than the stepped Ru(0001) surface. Specifically, 21 heteronuclear BACs display less negative U_L values, thus higher activity than their homonuclear counterparts.

We further computed PDOS of these 28 heteronuclear BACs and three homonuclear systems (Ti_2-Pc, V_2-Pc, and Re_2-Pc), and found that all these catalysts are metallic (**Figure S13**). Note that the metallicity can ensure the high carrier mobility during the reaction process. The superior catalytic activity, as well as the metallic characteristic could render these BACs as promising efficient catalysts towards NRR. In the following sections, we will focus on the catalytic selectivity of these 31 NRR catalysts (28 heteronuclear and three homonuclear).

3.4. Selectivity Evaluation of NRR Catalysts

Besides the high stability and activity, an ideal catalyst for N_2 fixation should be able to effectively suppress HER to achieve the high FE for the production of NH_3. Therefore, our final step is to quantify the catalytic selectivity of the screened catalysts.

Basically, since the adsorption free energy of H adsorbate ($\Delta G(H^*)$) is commonly more negative than that for N_2* on most metal surfaces,[92] H* can easily cover the metal surfaces and block active sites for NRR. Especially, due to the involvement of proton and electron transfer in H adsorption, the H adsorption process can be facilitated by the negative electrode potential. On the contrary, the free energy of N_2 adsorption is insensitive to the electrode potential due to the lack of proton and electron transfer during the N_2 adsorption. Thus, with increasing electrode potential (more negative), the HER could dominate the reaction process until the adsorption of N_2H* is favored. In this context, we calculated the free energy difference between the H* and N_2H* ($\Delta G(H^*) - \Delta G(N_2H^*)$) to estimate the catalytic selectivity of different catalysts.

The $\Delta G(H^*) - \Delta G(N_2H^*)$ versus U_L relationship for the 31 promising NRR catalysts (three homonuclear and 28 heteronuclear BACs) is presented in **Figure 6**, and the relevant data for the six reported high-performance NRR catalysts, i.e., B-C_3N_4,[43], Mo-C_2N,[94] Mo-GDY[49], Ru-N_3,[50] Ru-NC_2, and Ru-ZrO_2,[96] are given for comparison. To exclude the possible deviation in different studies, all the theoretical results were obtained at the same theoretical level (DFT-D3, more details in Supporting Information). Based on this selectivity criterion, a catalyst with a positive $\Delta G(H^*) - \Delta G(N_2H^*)$ value (>0) suggests a significant preference for hydrogenation of N_2*, thus possesses the good selectivity.

However, the calculated $\Delta G(H^*) - \Delta G(N_2H^*)$ values of most considered 31 BACs and all the reported reference catalysts are below zero, implying the strong competition of HER during the reaction process. Specifically, our computations

suggested that there exists a trade-off between adsorption of N_2H^* and H*, as catalysts with strong binding for N_2H^* also involves the strong capability for H* adsorption, leading to the poor selectivity under the reaction conditions (**Figure S14**). Remarkably, five systems, namely Ti_2-Pc, V_2-Pc, TiV-Pc, VCr-Pc, and VTa-Pc, have positive or roughly neutral $\Delta G(H^*) - \Delta G(N_2H^*)$ values (0.04, −0.07, 0.01, −0.07 and 0.09 eV, respectively), thus are expected to be able to (nearly) eliminate HER, and exhibit the highest selectivity for NRR.

Note that the (non-zero) charge and hydrogen bonding between the polar reaction intermediates and the H_2O could affect the binding strength of reaction intermediates on catalysts, especially in 2D materials.[99] However, the most important criteria for us to evaluate the activity and selectivity of the NRR electrocatalysts, namely the U_L and the N_2H and H* ($\Delta G(H^*) - \Delta G(N_2H^*)$, are obtained by comparing the energies of two or multiple intermediates, and the energy change caused by charges and solvation on the reaction species commonly are in the same degree,[100,101] leading to "error cancellation.

On the other hand, once electrode potentials are set, the oxidation of metal centers might be a problem for NRR, especially Ti or V are oxophylic and BAC surface might be covered with -OH or -O under NRR and HER conditions. To address this potential problem, we systematically investigated the possible deoxidation/dehydroxylation process (by hydrogenating the O*/OH* functional groups) on the high-performance NRR catalysts we screened out, i.e., the Ti_2-Pc, V_2-Pc, TiV-Pc, VCr-Pc, and VTa-Pc surfaces (**Figure S15).**

On all these five catalysts, when oxygen is attached, the O* can be easily protonated to OH* by the H^+/e^- pair with the downhill energies of between −0.52 and −1.62 eV. Further protonation of OH* can lead to the formation of H_2O* with downhill energy of −0.36 eV on VCr-Pc), or by overcoming the accessible energy barrier of 0.38, 0.55, and 0.35 eV, respectively, on Ti_2-Pc, V_2-Pc, TiV-Pc, which are well below 0.75 eV, commonly considered to be surmountable for reactions at room temperature.[102] Thus, on these four BACs, the surface oxidation or hydroxylation is not a big concern. However, on the VTa-Pc surface, the protonation of OH* to H_2O* could be suppressed due to the high energy demand of 1.22 eV, and a more negative potential needs to be applied to favor H_2O* formation. Consequently, for NRR under the alkaline conditions (i.e. containing high levels of hydroxyl), the OH* may constantly occupy the active sites of the VTa-Pc surface, leading to the reduced activity for NH_3 production, the possible oxidation of active sites on this catalyst should be taken into account.

Nevertheless, the possible surface oxidation and proton transfer can be reduced by a few experimental strategies, such as developing gas-diffusion-electrode flow cells with a controlled local liquid/gas environment,[103] operating three phase interfaces (electrolyte/ electrode/ gas) by a superhydrophobic coating layer to optimize the local environment and mass transfer,[104] and using the nonaqueous electrolytes to dilute the water concentration and thus reduce the proton donor activity.[105-106] Guided by these encouraging findings, it is expected that similar strategies could be used to attenuate HER or surface oxidation on the BACs.

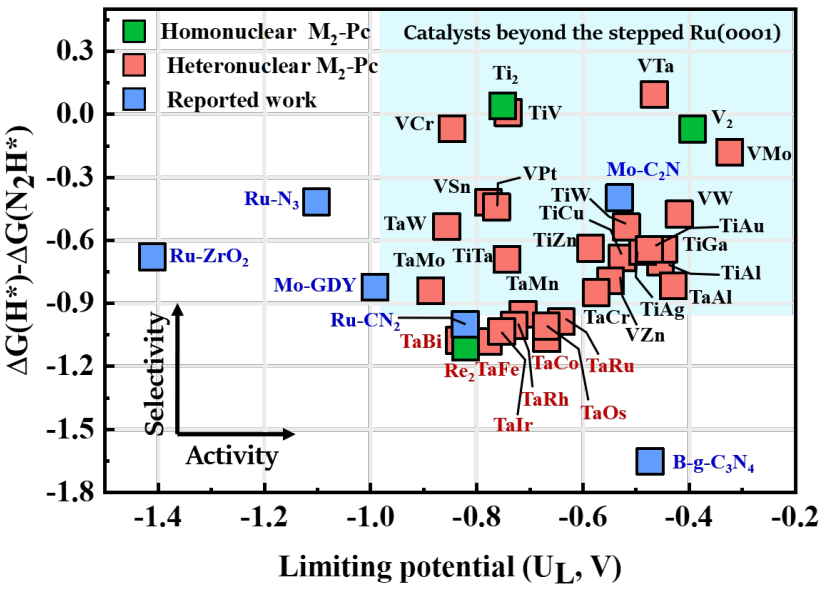

Figure 6. Limiting potential (U_L) versus $\Delta G(H^*) - \Delta G(N_2H^*)$ on 31 M_2-Pc and six reported catalysts.

4. CONCLUSIONS

In summary, by means of DFT computations, we systematically examined the potential of a branch of 2D BACs, namely M_2-Pc and MM'-Pc, as efficient N_2 fixation electrocatalysts. Taking advantage of the activity descriptor (N_2H^* adsorption energy), we surveyed a large composition space of homonuclear M_2-Pc BACs as well as their heteronuclear counterparts (MM'-Pc, with over 900 candidates), and investigated the catalytic activity of the promising catalysts towards NRR. Three homonuclear BACs and 28 heteronuclear catalysts were identified as highly active NRR catalysts under the electrochemical conditions. Particularly, five systems, including Ti_2-Pc, V_2-Pc, TiV-Pc, VCr-Pc, and VTa-Pc, can effectively suppress the competitive HER with favorable limiting potential of −0.75, −0.39, −0.74, −0.85 and −0.47 V, surpassing most of the reported electrocatalysts at the acid conditions. Overall, this work not only gain us a

comprehensive understanding of the stability, activity, and selectivity of M_2-Pc/MM'-Pc electrocatalysts, but also provide an effective strategy for screening and designing novel BACs for NRR. We believe this work will motivate more experimental and theoretical efforts to further explore the potential of two-dimensional BACs for NRR and other related electrochemical reactions.

AUTHOR INFORMATION

Supporting Information

Computational methods of Gibbs free energy and kinetic computations; Descriptions of surface models; Effects of DFT+U on reaction species; Structural parameters, computed cohesive energies, formation energies and dissolution potential of metal atoms for 30 homonuclear M_2-Pc; Computed vibrational frequencies, zero-point energies and entropy of reaction intermediates on Ti_2-Pc, V_2-Pc, Re_2-Pc, and eight reported catalysts (i.e., B-C_3N_4, Mo-C_2N, Mo-GDY, Ru-N_3, Ru-NC_2, and Ru-ZrO_2); Summary of NH_3* adsorption energies ($\Delta G_{NH_3^*}$) on 31 BACs which were screened out by activity analysis; Summary of $\Delta E_{N_2H^*}$, U_L, PDS, $\Delta G_{N_2^*}$, and ΔG_{H^*}, on 37 heteronuclear MM'-Pc; Total energies and thermodynamic quantities for the gas phase N_2, H_2, NH_3 species; Optimized structures and binding energies of Fe dimers anchored on 2D materials; Optimized structures of 30 homonuclear M_2-Pc; Bond lengths of metal dimers in M_2-Pc and the corresponding bulk phases; Formation energy versus dissolution potential of the experimentally available SACs; ICOHP versus the free energy change of the first elementary step for NRR; Reaction pathway of N_2 dissociation on Ta_2-Pc surface; Optimized structures of reaction intermediate on Ti_2-Pc, V_2-Pc, and Re_2-Pc; Optimized structures and related kinetic barriers of the reduction of NH_2* to NH_3* on Ti_2-Pc and V_2-Pc surfaces; Correlation between the $\Delta E_{NH_2^*}$ and $\Delta E_{N_2H^*}$ as well as the U_L on 25 homonuclear BACs; Correlations between the $\Delta E_{N_2H^*}$ and the band center of adsorbed metal atoms as well as the ε_{LUS} of 25 homonuclear

BACs; DOS of three homonuclear M_2-Pc and 28 heteronuclear MM'-Pc; Relations between $\Delta G_{N_2H^*}$ and ΔG_{H^*} on 31 MM'-Pc systems screened out by activity analysis; Relative free energy changes along the deoxidation/dehydroxylation process on the Ti_2-Pc, V_2-Pc, TiV-Pc, VCr-Pc, and VTa-Pc surfaces at the potential of U_L; NRR pathways on the Ti_2-Pc and DOS of Ti_2-Pc by using DFT and DFT+U methods.

Corresponding Author

* zhangslvip@njust.edu.cn (SZ)

* huangsp@mail.buct.edu.cn (SH)

* zhongfangchen@gmail.com (ZC)

ORCID

Zhongfang Chen: 0000-0002-1445-9184

Shengli Zhang: 0000-0003-4981-231X

Xiangyu Guo: 0000-0001-5102-2910

Jinxing Gu: 0000-0003-4805-7017

Shiru Lin: 0000-0002-0159-2269

Notes

The authors declare no competing financial interest.

ACKNOWLEDGMENTS

This work is supported in China by the National Natural Science Foundation of China (Grant No. 21776004), the Fundamental Research Funds for the Central Universities (No. 30916015106) and in USA by the National Science Foundation-Centers of Research Excellence in Science and Technology (NSF-CREST Center) for Innovation,

Research and Education in Environmental Nanotechnology (CIRE2N) (Grant No. HRD-1736093).

REFERENCES

1. Chen, J. G.; Crooks, R. M.; Seefeldt, L. C.; Bren, K. L.; Bullock, R. M.; Darensbourg, M. Y.; Holland, P. L.; Hoffman, B.; Janik, M. J.; Jones, A. K.; Kanatzidis, M. G.; King, P.; Lancaster, K. M.; Lymar, S. V.; Pfromm, P.; Schneider, W. F.; Schrock, R. R. Beyond Fossil Fuel–Driven Nitrogen Transformations. *Science* **2018,** *360*, 6611-6617.
2. Foster, S. L.; Bakovic, S. I. P.; Duda, R. D.; Maheshwari, S.; Milton, R. D.; Minteer, S. D.; Janik, M. J.; Renner, J. N.; Greenlee, L. F. Catalysts for Nitrogen Reduction to Ammonia. *Nat. Catal.* **2018,** *1*, 490-500.
3. Seh, Z. W.; Kibsgaard, J.; Dickens, C. F.; Chorkendorff, I.; Nørskov, J. K.; Jaramillo, T. F. Combining Theory and Experiment in Electrocatalysis: Insights into Materials Design. *Science* **2017,** *355*, 4998-5009.
4. Soloveichik, G. Electrochemical Synthesis of Ammonia as a Potential Alternative to the Haber–Bosch Process. *Nat. Catal.* **2019,** *2*, 377-380.
5. Martín, A. J.; Shinagawa, T.; Pérez-Ramírez, J. Electrocatalytic Reduction of Nitrogen: From Haber-Bosch to Ammonia Artificial Leaf. *Chem* **2019,** *5*, 263-283.
6. Yin, H.; Dou, Y.; Chen, S.; Zhu, Z.; Liu, P.; Zhao, H. 2D Electrocatalysts for Converting Earth-Abundant Simple Molecules into Value-Added Commodity Chemicals: Recent Progress and Perspectives. *Adv. Mater.* **2019**, 1904870-1904901.

https://doi.org/10.1002/adma.201904870

7. Kyriakou, V.; Garagounis, I.; Vourros, A.; Vasileiou, E.; Stoukides, M. An Electrochemical Haber-Bosch Process. *Joule* **2019, 4,** 142-158.

8. Guo, W.; Zhang, K.; Liang, Z.; Zou, R.; Xu, Q. Electrochemical nitrogen fixation and utilization: theories, advanced catalyst materials and system design. *Chem. Soc. Rev.* **2019,** 48, 5658-5716.

9. Singh, A. R.; Rohr, B. A.; Schwalbe, J. A.; Cargnello, M.; Chan, K.; Jaramillo, T. F.; Chorkendorff, I.; Nørskov, J. K. Electrochemical Ammonia Synthesis—The Selectivity Challenge. *ACS Catal.* **2017,** *7*, 706-709.

10. Minteer, S. D.; Christopher, P.; Linic, S. Recent Developments in Nitrogen Reduction Catalysts: A Virtual Issue. *ACS Energy Lett.* **2019,** *4*, 163-166.

11. Chen, G.; Ren, S.; Zhang, L.; Cheng, H.; Luo, Y.; Zhu, K.; Ding, L.; Wang, H. Advances in Electrocatalytic N_2 Reduction—Strategies to Tackle the Selectivity Challenge. *Small Methods* **2019**, 3, 1800337-1800356.

12. Suryanto, B. H. R.; Du, H.; Wang, D.; Chen, J.; Simonov, A. N.; MacFarlane, D. R. Challenges and Prospects in the Catalysis of Electroreduction of Nitrogen to Ammonia. *Nat. Catal.* **2019,** *2*, 290-296.

13. Singh, A. R.; Rohr, B. A.; Statt, M. J.; Schwalbe, J. A.; Cargnello, M.; Nørskov, J. K. Strategies toward Selective Electrochemical Ammonia Synthesis. *ACS Catal.* **2019,** *9*, 8316-8324.

14. Martín, A. J.; Pérez-Ramírez, J. Heading to Distributed Electrocatalytic Conversion of Small Abundant Molecules into Fuels, Chemicals, and Fertilizers.

Joule **2019,** 3, 2602-2621.

15. Guo, X.; Du, H.; Qu, F.; Li, J., Recent Progress in Electrocatalytic Nitrogen Reduction. *J. Mater. Chem. A* **2019,** 7, 3531-3543.
16. Wang, Y.; Shi, M.; Bao, D.; Meng, F.; Zhang, Q.; Zhou, Y.; Liu, K.; Zhang, Y.; Wang, J.; Chen, Z.; Liu, D.; Jiang, Z.; Luo, M.; Gu, L.; Zhang, Q.; Cao, X.; Yao, Y.; Shao, M.; Zhang, Y.; Zhang, X.; Chen, J. G.; Yan, J.; Jiang, Q. Generating Defect-Rich Bismuth for Enhancing the Rate of Nitrogen Electroreduction to Ammonia. *Angew. Chem. Int. Ed.* **2019,** *58*, 9464-9469.
17. Li, L.; Tang, C.; Xia, B.; Jin, H.; Zheng, Y.; Qiao, S. Z. Two-Dimensional Mosaic Bismuth Nanosheets for Highly Selective Ambient Electrocatalytic Nitrogen Reduction. *ACS Catal.* **2019,** *9*, 2902-2908.
18. Hao, Y.; Guo, Y.; Chen, L.; Shu, M.; Wang, X.; Bu, T.; Gao, W.; Zhang, N.; Su, X.; Feng, X.; Zhou, J.; Wang, B.; Hu, C.; Yin, A.; Si, R.; Zhang, Y.; Yan, C. Promoting Nitrogen Electroreduction to Ammonia with Bismuth Nanocrystals and Potassium Cations in Water. *Nat. Catal.* **2019,** 2, 448-456.
19. Yao, Y.; Zhu, S.; Wang, H.; Li, H.; Shao, M. A Spectroscopic Study on the Nitrogen Electrochemical Reduction Reaction on Gold and Platinum Surfaces. *J. Am. Chem. Soc.* **2018,** *140*, 1496-1501.
20. Yao, Y.; Wang, H.; Yuan, X. Z.; Li, H.; Shao, M. Electrochemical Nitrogen Reduction Reaction on Ruthenium. *ACS Energy Lett.* **2019,** *4*, 1336-1341.
21. Yang, Y.; Wang, S.; Wen, H.; Ye, T.; Chen, J.; Li, C.; Du, M. Nanoporous Gold Embedded ZIF Composite for Enhanced Electrochemical Nitrogen Fixation.

Angew. Chem. Int. Ed. **2019**, 131, 15506-15510.

22. Xue, Z.; Zhang, S.; Lin, Y.; Su, H.; Zhai, G.; Han, J.; Yu, Q.; Li, X.; Antonietti, M.; Chen, J. Electrochemical Reduction of N_2 into NH_3 by Donor-Acceptor Couples of Ni and Au Nanoparticles with a 67.8% Faradaic Efficiency. *J. Am. Chem. Soc.* **2019,** 141, 14976-14980.
23. Huang, L.; Wu, J.; Han, P.; Al-Enizi, A. M.; Almutairi, T. M.; Zhang, L.; Zheng, G. NbO_2 Electrocatalyst Toward 32% Faradaic Efficiency for N_2 Fixation. *Small Methods* **2019,** 3, 1800386-1800391.
24. Sun, Z.; Huo, R.; Choi, C.; Hong, S.; Wu, T.; Qiu, J.; Yan, C.; Han, Z.; Liu, Y.; Soo, Y.; Jung, Y. Oxygen Vacancy Enables Electrochemical N_2 Fixation over WO_3 with Tailored Structure. *Nano Energy* **2019,** *62*, 869-875.
25. Fang, Y.; Liu, Z.; Han, J.; Jin, Z.; Han, Y.; Wang, F.; Niu, Y.; Wu, Y.; Xu, Y. High-Performance Electrocatalytic Conversion of N_2 to NH_3 Using Oxygen-Vacancy-Rich TiO_2 In Situ Grown on $Ti_3C_2T_x$ MXene. *Adv. Energy Mater.* **2019,** *9*, 1803406-1803414.
26. Liu, Y.; Han, M.; Xiong, Q.; Zhang, S.; Zhao, C.; Gong, W.; Wang, G.; Zhang, H.; Zhao, H. Dramatically Enhanced Ambient Ammonia Electrosynthesis Performance by In-Operando Created Li–S Interactions on MoS_2 Electrocatalyst. *Adv. Energy Mater.* **2019,** *9*, 1803935-1803943.
27. Suryanto, B. H. R.; Wang, D.; Azofra, L. M.; Harb, M.; Cavallo, L.; Jalili, R.; Mitchell, D. R. G.; Chatti, M.; MacFarlane, D. R. MoS_2 Polymorphic Engineering Enhances Selectivity in the Electrochemical Reduction of Nitrogen to Ammonia.

ACS Energy Lett. **2018**, 430-435.

28. Qiu, W.; Xie, X. Y.; Qiu, J.; Fang, W. H.; Liang, R.; Ren, X.; Ji, X.; Cui, G.; Asiri, A. M.; Cui, G.; Tang, B.; Sun, X. High-Performance Artificial Nitrogen Fixation at Ambient Conditions using a Metal-free Electrocatalyst. *Nat. Commun.* **2018,** *9*, 3485-3492.
29. Zhang, X.; Wu, T.; Wang, H.; Zhao, R.; Chen, H.; Wang, T.; Wei, P.; Luo, Y.; Zhang, Y.; Sun, X. Boron Nanosheet: An Elemental Two-Dimensional (2D) Material for Ambient Electrocatalytic N_2-to-NH_3 Fixation in Neutral Media. *ACS Catal.* **2019,** *9*, 4609-4615.
30. Liu, S.; Wang, M.; Qian, T.; Ji, H.; Liu, J.; Yan, C. Facilitating Nitrogen Accessibility to Boron-Rich Covalent Organic Frameworks via Electrochemical Excitation for Efficient Nitrogen Fixation. *Nat. Commun.* **2019,** *10*, 3898-3906.
31. Zhang, L.; Ding, L.; Chen, G.; Yang, X.; Wang, H. Ammonia Synthesis Under Ambient Conditions: Selective Electroreduction of Dinitrogen to Ammonia on Black Phosphorus Nanosheets. *Angew. Chem. Int. Ed.* **2019,** 131, 2638-2642.
32. Zhao, S.; Lu, X.; Wang, L.; Gale, J.; Amal, R. Carbon-Based Metal-Free Catalysts for Electrocatalytic Reduction of Nitrogen for Synthesis of Ammonia at Ambient Conditions. *Adv. Mater.* **2019,** *31*, 1805367-1805375.
33. Yu, X.; Han, P.; Wei, Z.; Huang, L.; Gu, Z.; Peng, S.; Ma, J.; Zheng, G. Boron-Doped Graphene for Electrocatalytic N_2 Reduction. *Joule* **2018,** *2*, 1610-1622.
34. Ding, B.; Liu, Y.; Li, D.; Yu, J. Stable Confinement of Black Phosphorus Quantum Dots on Black Tin Oxide Nanotubes: A Robust, Double-Active Electrocatalyst

toward Efficient Nitrogen Fixation. *Angew. Chem. Int. Ed.* **2019,** 131, 16591-16596.

35. Yan, X.; Liu, D.; Cao, H.; Hou, F.; Liang, J.; Dou, S. X. Nitrogen Reduction to Ammonia on Atomic-Scale Active Sites under Mild Conditions. *Small Methods* **2019,** 3, 1800501-1800522.
36. Wang, Y.; Mao, J.; Meng, X.; Yu, L.; Deng, D.; Bao, X. Catalysis with Two-Dimensional Materials Confining Single Atoms: Concept, Design, and Applications. *Chem. Rev.* **2019,** *119*, 1806-1854.
37. Ding, S.; Hülsey, M. J.; Pérez-Ramírez, J.; Yan, N. Transforming Energy with Single-Atom Catalysts. *Joule* **2019,** 3, 2897-2929.
38. Pan, Y.; Zhang, C.; Liu, Z.; Chen, C.; Li, Y. Structural Regulation with Atomic-Level Precision: From Single-Atomic Site to Diatomic and Atomic Interface Catalysis. *Matter* **2020,** *2*, 78-110.
39. Li, Z.; Ji, S.; Liu, Y.; Cao, X.; Tian, S.; Chen, Y.; Niu, Z.; Li, Y. Well-Defined Materials for Heterogeneous Catalysis: From Nanoparticles to Isolated Single-Atom Sites. *Chem. Rev.* **2020,** *120*, 623-682.
40. Zhao, J.; Chen, Z. Single Mo Atom Supported on Defective Boron Nitride Monolayer as an Efficient Electrocatalyst for Nitrogen Fixation: A Computational Study. *J. Am. Chem. Soc.* **2017,** *139*, 12480-12487.
41. Guo, X.; Huang, S. Tuning Nitrogen Reduction Reaction Activity via Controllable Fe Magnetic Moment: A Computational Study of Single Fe Atom Supported on Defective Graphene. *Electrochim. Acta* **2018,** *284*, 392-399.
42. Liu, X.; Jiao, Y.; Zheng, Y.; Jaroniec, M.; Qiao, S. Z. Building Up a Picture of the

Electrocatalytic Nitrogen Reduction Activity of Transition Metal Single-Atom Catalysts. *J. Am. Chem. Soc.* **2019,** *141*, 9664-9672.

43. Ling, C.; Niu, X.; Li, Q.; Du, A.; Wang, J. Metal-Free Single Atom Catalyst for N_2 Fixation Driven by Visible Light. *J. Am. Chem. Soc.* **2018,** *140*, 14161-14168.
44. Lv, X.; Wei, W.; Li, F.; Huang, B.; Dai, Y. Metal-Free B@g-CN: Visible/Infrared Light-Driven Single Atom Photocatalyst Enables Spontaneous Dinitrogen Reduction to Ammonia. *Nano Lett.* **2019,** *19*, 6391-6399.
45. Liu, C.; Li, Q.; Wu, C.; Zhang, J.; Jin, Y.; MacFarlane, D. R.; Sun, C. Single-Boron Catalysts for Nitrogen Reduction Reaction. *J. Am. Chem. Soc.* **2019,** *141*, 2884-2888.
46. Wang, M.; Liu, S.; Qian, T.; Liu, J.; Zhou, J.; Ji, H.; Xiong, J.; Zhong, J.; Yan, C. Over 56.55% Faradaic Efficiency of Ambient Ammonia Synthesis Enabled by Positively Shifting the Reaction Potential. *Nat. Commun.* **2019,** *10*, 341-348.
47. Han, L.; Liu, X.; Chen, J.; Lin, R.; Liu, H.; Lü, F.; Bak, S.; Liang, Z.; Zhao, S.; Stavitski, E.; Luo, J.; Adzic, R. R.; Xin, H. L. Atomically Dispersed Molybdenum Catalysts for Efficient Ambient Nitrogen Fixation. *Angew. Chem. Int. Ed.* **2019,** 58, 2321-2325.
48. He, C.; Wu, Z.-Y.; Zhao, L.; Ming, M.; Zhang, Y.; Yi, Y.; Hu, J. S. Identification of FeN_4 as an Efficient Active Site for Electrochemical N_2 Reduction. *ACS Catal.* **2019**, 9, 7311-7317.
49. Hui, L.; Xue, Y.; Yu, H.; Liu, Y.; Fang, Y.; Xing, C.; Huang, B.; Li, Y. Highly Efficient and Selective Generation of Ammonia and Hydrogen on a Graphdiyne-

Based Catalyst. *J. Am. Chem. Soc.* **2019,** *141*, 10677-10683.

50. Geng, Z.; Liu, Y.; Kong, X.; Li, P.; Li, K.; Liu, Z.; Du, J.; Shu, M.; Si, R.; Zeng, J. Achieving a Record-High Yield Rate of 120.9 $\mu g_{NH_3}\, mg_{cat.}^{-1}\, h^{-1}$ for N_2 Electrochemical Reduction over Ru Single-Atom Catalysts. *Adv. Mater.* **2018,** 30, 1803498-1803503.
51. Jiao, J.; Lin, R.; Liu, S.; Cheong, W.; Zhang, C.; Chen, Z.; Pan, Y.; Tang, J.; Wu, K.; Hung, S.; Chen, H.; Zheng, L.; Lu, Q.; Yang, X.; Xu, B.; Xiao, H.; Li, J.; Wang, D.; Peng, Q.; Chen, C.; Li, Y. Copper Atom-pair Catalyst Anchored on Alloy Nanowires for Selective and Efficient Electrochemical Reduction of CO_2. *Nat. Chem.* **2019,** *11*, 222-228.
52. An, B.; Li, Z.; Song, Y.; Zhang, J.; Zeng, L.; Wang, C.; Lin, W. Cooperative Copper Centres in a Metal–Organic Framework for Selective Conversion of CO_2 to Ethanol. *Nat. Catal.* **2019**, 2, 709-717.
53. Li, X.; Sun, Y.; Xu, J.; Shao, Y.; Wu, J.; Xu, X.; Pan, Y.; Ju, H.; Zhu, J.; Xie, Y. Selective Visible-Light-Driven Photocatalytic CO_2 Reduction to CH_4 Mediated by Atomically thin $CuIn_5S_8$ layers. *Nat. Energy* **2019**, 4, 690-699.
54. Cao, N.; Chen, Z.; Zang, K.; Xu, J.; Zhong, J.; Luo, J.; Xu, X.; Zheng, G. Doping Strain Induced Bi-Ti^{3+} Pairs for Efficient N_2 Activation and Electrocatalytic Fixation. *Nat. Commun.* **2019,** *10*, 2877-2888.
55. Ye, W.; Chen, S.; Lin, Y.; Yang, L.; Chen, S.; Zheng, X.; Qi, Z.; Wang, C.; Long, R.; Chen, M.; Zhu, J.; Gao, P.; Song, L.; Jiang, J.; Xiong, Y. Precisely Tuning the Number of Fe Atoms in Clusters on N-Doped Carbon toward Acidic Oxygen

Reduction Reaction. *Chem* **2019,** 5, 2865-2878.

56. Pérez-Ramírez, J.; López, N. Strategies to Break Linear Scaling Relationships. *Nat. Catal.* **2019,** 2, 971–976

57. Yan, H.; Lin, Y.; Wu, H.; Zhang, W.; Sun, Z.; Cheng, H.; Liu, W.; Wang, C.; Li, J.; Huang, X.; Yao, T.; Yang, J.; Wei, S.; Lu, J. Bottom-Up Precise Synthesis of Stable Platinum Dimers on Graphene. *Nat. Commun.* **2017,** *8*, 1070-1080.

58. Li, X.; Zhong, W.; Cui, P.; Li, J.; Jiang, J. Design of Efficient Catalysts with Double Transition Metal Atoms on C_2N Layer. *J. Phys. Chem. Lett.* **2016,** *7*, 1750-1755.

59. Hunter, M. A.; Fischer, J. M. T. A.; Yuan, Q.; Hankel, M.; Searles, D. J. Evaluating the Catalytic Efficiency of Paired, Single-Atom Catalysts for the Oxygen Reduction Reaction. *ACS Catal.* **2019**, 9, 7660-7667.

60. Zhang, X.; Chen, A.; Zhang, Z.; Zhou, Z. Double-Atom Catalysts: Transition Metal Dimer-Anchored C_2N Monolayers as N_2 Fixation Electrocatalysts. *J. Mater. Chem. A* **2018,** *6*, 18599-18604.

61. Chen, Z.; Yan, J.; Jiang, Q. Single or Double: Which Is the Altar of Atomic Catalysts for Nitrogen Reduction Reaction? *Small Methods* **2019**, 3, 1800291-1800298.

62. Zhou, P.; Hou, X.; Chao, Y.; Yang, W.; Zhang, W.; Mu, Z.; Lai, J.; Lv, F.; Yang, K.; Liu, Y.; Li, J.; Ma, J.; Luo, J.; Guo, S. Synergetic Interaction between Neighboring Platinum and Ruthenium Monomers boosts CO oxidation. *Chem. Sci.* **2019,** *10*, 5898-5905.

63. Ren, W.; Tan, X.; Yang, W.; Jia, C.; Xu, S.; Wang, K.; Smith, S. C.; Zhao, C.

Isolated Diatomic Ni-Fe Metal–Nitrogen Sites for Synergistic Electroreduction of CO_2. *Angew. Chem. Int. Ed.* **2019,** *58*, 6972-6976.

64. Li, F.; Liu, X.; Chen, Z. 1 + 1′ > 2: Heteronuclear Biatom Catalyst Outperforms Its Homonuclear Counterparts for CO Oxidation. *Small Methods* **2019,** 3, 1800480-1800488.

65. Lu, Z.; Wang, B.; Hu, Y.; Liu, W.; Zhao, Y.; Yang, R.; Li, Z.; Luo, J.; Chi, B.; Jiang, Z.; Li, M.; Mu, S.; Liao, S.; Zhang, J.; Sun, X. An Isolated Zinc–Cobalt Atomic Pair for Highly Active and Durable Oxygen Reduction. *Angew. Chem. Int. Ed.* **2019,** *58*, 2622-2626.

66. Li, Y.; Zhang, Q.; Li, C.; Fan, H.; Luo, W.; Liu, H.; Shixue, D., Atomically Dispersed Metal Dimer Species with Selective Catalytic Activity for Nitrogen Electrochemical Reduction. *J. Mater. Chem. A* **2019,** 7, 22242-22247.

67. Han, X.; Ling, X.; Yu, D.; Xie, D.; Li, L.; Peng, S.; Zhong, C.; Zhao, N.; Deng, Y.; Hu, W. Atomically Dispersed Binary Co-Ni Sites in Nitrogen-Doped Hollow Carbon Nanocubes for Reversible Oxygen Reduction and Evolution. *Adv. Mater.* **2019,** 31, 1905622-1905630.

68. Zhang, L.; Si, R.; Liu, H.; Chen, N.; Wang, Q.; Adair, K.; Wang, Z.; Chen, J.; Song, Z.; Li, J.; Banis, M. N.; Li, R.; Sham, T. K.; Gu, M.; Liu, L.-M.; Botton, G. A.; Sun, X. Atomic Layer Deposited Pt-Ru Dual-Metal Dimers and Identifying Their Active Sites for Hydrogen Evolution Reaction. *Nat. Commun.* **2019,** 10, 4936-4946.

69. Zhu, X.; Yan, J.; Gu, M.; Liu, T.; Dai, Y.; Gu, Y.; Li, Y. Activity Origin and Design Principles for Oxygen Reduction on Dual-Metal-Site Catalysts: A Combined

Density Functional Theory and Machine Learning Study. *J. Phys. Chem. Lett.* **2019,** *10*, 7760-7766.

70. Ouyang, Y.; Shi, L.; Bai, X.; Li, Q.; Wang, J. Breaking scaling relations for efficient CO2 electrochemical reduction through dual-atom catalysts. *Chem. Sci.* **2020**. https://doi.org/10.1039/C9SC05236D
71. Blöchl, P. E. Projector Augmented-Wave Method. *Phy. Rev. B* **1994,** *50*, 17953-17979.
72. Grimme, S. Semiempirical GGA-type Density Functional Constructed with a Long-Range Dispersion Correction. *J. Comput. Chem.* **2006,** *27*, 1787-1799.
73. Perdew, J. P.; Burke, K.; Ernzerhof, M. Generalized Gradient Approximation Made Simple. *Phys. Rev. Lett.* **1996,** *77*, 3865-3868.
74. Montoya, J. H.; Tsai, C.; Vojvodic, A.; Nørskov, J. K. The Challenge of Electrochemical Ammonia Synthesis: A New Perspective on the Role of Nitrogen Scaling Relations. *ChemSusChem* **2015,** *8*, 2180-2186.
75. Nørskov, J. K.; Rossmeisl, J.; Logadottir, A.; Lindqvist, L.; Kitchin, J. R.; Bligaard, T.; Jónsson, H. Origin of the Overpotential for Oxygen Reduction at a Fuel-Cell Cathode. *J. Phys. Chem. B* **2004,** *108*, 17886-17892.
76. He, Z.; He, K.; Robertson, A. W.; Kirkland, A. I.; Kim, D.; Ihm, J.; Yoon, E.; Lee, G.-D.; Warner, J. H. Atomic Structure and Dynamics of Metal Dopant Pairs in Graphene. *Nano Lett.* **2014,** *14*, 3766-3772.
77. Tian, S.; Fu, Q.; Chen, W.; Feng, Q.; Chen, Z.; Zhang, J.; Cheong, W. C.; Yu, R.; Gu, L.; Dong, J.; Luo, J.; Chen, C.; Peng, Q.; Draxl, C.; Wang, D.; Li, Y. Carbon

Nitride Supported Fe_2 Cluster Catalysts with Superior Performance for Alkene Epoxidation. *Nat. Commun.* **2018,** *9*, 2353-2359.

78. Vorobyeva, E.; Fako, E.; Chen, Z.; Collins, S. M.; Johnstone, D.; Midgley, P. A.; Hauert, R.; Safonova, O. V.; Vilé, G.; López, N.; Mitchell, S.; Pérez-Ramírez, J. Atom-by-Atom Resolution of Structure–Function Relations over Low-Nuclearity Metal Catalysts. *Angew. Chem. Int. Ed.* **2019**, 58, 8724-8729.
79. Zhang, L.; Fischer, J. M. T. A.; Jia, Y.; Yan, X.; Xu, W.; Wang, X.; Chen, J.; Yang, D.; Liu, H.; Zhuang, L.; Hankel, M.; Searles, D. J.; Huang, K.; Feng, S.; Brown, C. L.; Yao, X. Coordination of Atomic Co–Pt Coupling Species at Carbon Defects as Active Sites for Oxygen Reduction Reaction. *J. Am. Chem. Soc.* **2018,** *140*, 10757-10763.
80. Xiao, M.; Chen, Y.; Zhu, J.; Zhang, H.; Zhao, X.; Gao, L.; Wang, X.; Zhao, J.; Ge, J.; Jiang, Z.; Chen, S.; Liu, C.; Xing, W. Climbing the Apex of the ORR Volcano Plot via Binuclear Site Construction: Electronic and Geometric Engineering. *J. Am. Chem. Soc.* **2019,** 141, 17763-17770.
81. Matsushita, O.; Derkacheva, V. M.; Muranaka, A.; Shimizu, S.; Uchiyama, M.; Luk'yanets, E. A.; Kobayashi, N. Rectangular-Shaped Expanded Phthalocyanines with Two Central Metal Atoms. *J. Am. Chem. Soc.* **2012,** *134*, 3411-3418.
82. Li, Q. K.; Li, X. F.; Zhang, G.; Jiang, J. Cooperative Spin Transition of Monodispersed FeN_3 Sites within Graphene Induced by CO Adsorption. *J. Am. Chem. Soc.* **2018,** *140*, 15149-15152.
83. Greeley, J.; Nørskov, J. K. Electrochemical Dissolution of Surface Alloys in Acids:

Thermodynamic Trends from First-Principles Calculations. *Electrochim. Acta* **2007,** *52*, 5829-5836.

84. Guo, X.; Lin, S.; Gu, J.; Zhang, S.; Chen, Z.; Huang, S. Simultaneously Achieving High Activity and Selectivity toward Two-Electron O_2 Electroreduction: The Power of Single-Atom Catalysts. *ACS Catal.* **2019,** 11042-11054.
85. Chatt, J.; Dilworth, J. R.; Richards, R. L. Recent Advances in the Chemistry of Nitrogen Fixation. *Chem. Rev.* **1978,** *78*, 589-625.
86. Seefeldt, L. C.; Hoffman, B. M.; Dean, D. R. Mechanism of Mo-Dependent Nitrogenase. *Annu. Rev. Biochem.* **2009,** *78*, 701-722.
87. Hinnemann, B.; Nørskov, J. K. Catalysis by Enzymes: the Biological Ammonia Synthesis. *Top. Catal.* **2006,** *37*, 55-70.
88. Anderson, J. S.; Rittle, J.; Peters, J. C. Catalytic Conversion of Nitrogen to Ammonia by an Iron Model Complex. *Nature* **2013,** 501, 84-88.
89. Maintz, S.; Deringer, V. L.; Tchougréeff, A. L.; Dronskowski, R. LOBSTER: A Tool to Extract Chemical Bonding from Plane-Wave Based DFT. *J. Comput. Chem.* **2016,** *37*, 1030-1035.
90. Ling, C.; Ouyang, Y.; Li, Q.; Bai, X.; Mao, X.; Du, A.; Wang, J. A General Two-Step Strategy–Based High-Throughput Screening of Single Atom Catalysts for Nitrogen Fixation. *Small Methods* **2018,** 3, 1800376-1800383.
91. Skulason, E.; Bligaard, T.; Gudmundsdottir, S.; Studt, F.; Rossmeisl, J.; Abild-Pedersen, F.; Vegge, T.; Jonsson, H.; Nørskov, J. K. A Theoretical Evaluation of Possible Transition Metal Electro-Catalysts for N_2 Reduction. *Phys. Chem. Chem.*

Phys. **2012,** *14*, 1235-1245.

92. Choi, C.; Back, S.; Kim, N.-Y.; Lim, J.; Kim, Y. H.; Jung, Y. Suppression of Hydrogen Evolution Reaction in Electrochemical N_2 Reduction Using Single-Atom Catalysts: A Computational Guideline. *ACS Catal.* **2018,** *8*, 7517-7525.
93. Chun, H. J.; Apaja, V.; Clayborne, A.; Honkala, K.; Greeley, J. Atomistic Insights into Nitrogen-Cycle Electrochemistry: A Combined DFT and Kinetic Monte Carlo Analysis of NO Electrochemical Reduction on Pt(100). *ACS Catal.* **2017,** *7*, 3869-3882.
94. Katsounaros, I.; Figueiredo, M. C.; Chen, X.; Calle-Vallejo, F.; Koper, M. T. M. Structure- and Coverage-Sensitive Mechanism of NO Reduction on Platinum Electrodes. *ACS Catal.* **2017,** *7*, 4660-4667.
95. Wang, Z.; Yu, Z.; Zhao, J. Computational Screening of a Single Transition Metal Atom Supported on the C_2N Monolayer for Electrochemical Ammonia Synthesis. *Phys. Chem. Chem. Phys.* **2018,** *20*, 12835-12844.
96. Tao, H.; Choi, C.; Ding, L. X.; Jiang, Z.; Han, Z.; Jia, M.; Fan, Q.; Gao, Y.; Wang, H.; Robertson, A. W.; Hong, S.; Jung, Y.; Liu, S.; Sun, Z. Nitrogen Fixation by Ru Single-Atom Electrocatalytic Reduction. *Chem* **2019,** *5*, 204-214.
97. Liu, Y.; Wang, Y. M.; Yakobson, B. I.; Wood, B. C. Assessing Carbon-Based Anodes for Lithium-Ion Batteries: A Universal Description of Charge-Transfer Binding. *Phys. Rev. Lett.* **2014,** *113*, 028304.
98. Liu, Y.; Wu, J.; Hackenberg, K. P.; Zhang, J.; Wang, Y. M.; Yang, Y.; Keyshar, K.; Gu, J.; Ogitsu, T.; Vajtai, R.; Lou, J.; Ajayan, P. M.; Wood, Brandon C.; Yakobson,

B. I. Self-optimizing, Highly Surface-Active Layered Metal Dichalcogenide Catalysts for Hydrogen Evolution. *Nat. Energy* **2017,** *2*, 17127-17133.

99. Kim, D.; Shi, J.; Liu, Y. Substantial Impact of Charge on Electrochemical Reactions of Two-Dimensional Materials. *J. Am. Chem. Soc.* **2018,** *140*, 9127-9131.

100. Ping, Y.; Nielsen, R. J.; Goddard, W. A. The Reaction Mechanism with Free Energy Barriers at Constant Potentials for the Oxygen Evolution Reaction at the IrO_2 (110) Surface. *J. Am. Chem. Soc.* **2017,** *139*, 149-155

101. Zhang, H.; Goddard, W. A.; Lu, Q.; Cheng, M.-J. The importance of grand-canonical quantum mechanical methods to describe the effect of electrode potential on the stability of intermediates involved in both electrochemical CO_2 reduction and hydrogen evolution. *Phys. Chem. Chem. Phys.* **2018,** *20*, 2549-2557.

102. Wang, H.; Liu, Z. Comprehensive Mechanism and Structure-Sensitivity of Ethanol Oxidation on Platinum: New Transition-State Searching Method for Resolving the Complex Reaction Network. *J. Am. Chem. Soc.* **2008,** *130*, 10996-11004.

103. Hu, L.; Xing, Z.; Feng, X. Understanding the Electrocatalytic Interface for Ambient Ammonia Synthesis. *ACS Energy Lett.* **2020**, 430-436.

104. Lee, H. K.; Koh, C. S. L.; Lee, Y. H.; Liu, C.; Phang, I. Y.; Han, X.; Tsung, C.-K.; Ling, X. Y. Favoring the Unfavored: Selective Electrochemical Nitrogen Fixation using a Reticular Chemistry Approach. *Sci. Adv.* **2018,** *4*, 3208-3215.

105. Zhou, F.; Azofra, L. M.; Ali, M.; Kar, M.; Simonov, A. N.; McDonnell-Worth, C.; Sun, C.; Zhang, X.; MacFarlane, D. R. Electro-Synthesis of Ammonia from

Nitrogen at Ambient Temperature and Pressure in Ionic Liquids. *Energy Environ. Sci.* **2017,** *10*, 2516-2520.

106. Suryanto, B. H. R.; Kang, C. S. M.; Wang, D.; Xiao, C.; Zhou, F.; Azofra, L. M.; Cavallo, L.; Zhang, X.; MacFarlane, D. R. Rational Electrode–Electrolyte Design for Efficient Ammonia Electrosynthesis under Ambient Conditions. *ACS Energy Lett.* **2018,** *3*, 1219-1224.

TOC Graphic